Chapter IV:

Geophysical Implications of Izu-Bonin Mantle Wedge Hydration from Chemical Geodynamic Modeling

Laura Baker Hebert and Michael Gurnis

Abstract

Using two-dimensional (2-D) dynamic models of the Northern Izu-Bonin (NIB) subduction zone, we show that a particular localized low-viscosity ($\eta_{LV} = 3.3\times10^{19}$-$4.0\times10^{20}$ Pa s), low-density ($\Delta\rho \sim$ -10 kg/m^3 relative to ambient mantle) geometry within the wedge is required to match surface observations of topography, gravity, and geoid anomalies. The hydration structure resulting in this low-viscosity, low-density geometry was produced via coupled geochemical and geodynamic modeling of the NIB subduction system with GyPSM-S (**G**eo**dy**namic and **P**etrological **S**ynthesis **M**odel for **S**ubduction, Chapter 2). First-order controls on the geometry of hydration within the wedge arise from the thermal structure of the down going slab (mostly a function of slab age), slab dip angle, the mechanism of fluid transport within the wedge, and the spatial position of the water-saturated solidus within the wedge. Slab convergence velocity is a second-order control on the geometry of the hydrated region. On the basis of this modeling, predictions can be made as to the specific low-viscosity geometries associated with geophysical surface observables for other subduction zones based on regional subduction parameters.

Keywords: viscosity, topography, geoid, gravity, Izu-Bonin, water, nominally anhydrous minerals, wedge, GyPSM-S

1. Introduction

Convergent margin volcanism can be explained in terms of the addition of volatiles from the dehydrating slab to the overlying mantle wedge, leading to water-fluxed melting. The locations of dehydration reactions within the slab are dependent on the thermal structure, which is defined primarily by the age of the plate (Chapter 3). Infiltration and equilibration of hydrous fluids with the wedge peridotite allows for increasing amounts of water to be stabilized in nominally anhydrous minerals (NAM) such as olivine, garnet, orthopyroxene, and clinopyroxene [1], as well as for the appearance of hydrous phases such as amphibole, antigorite, chrysotile, and chlorite [2-5]. The effect of increasing water content in NAM is twofold: (i) decreasing solidus temperatures [6, 7] and (ii) water-weakening that reduces the viscosity of the solid material [8]. As such, there is a dual effect of hydrous fluid introduction on the geochemistry of initial melts within the system (Chapter 3) and on the force balance within the wedge. Previous modeling studies [2, 4, 9, 10] have addressed the role of water and wedge hydration in the subduction system together with dynamical considerations, emphasizing the role of hydrous minerals in acting as transport agents and/or sources of water and using phase diagram parameterization to approximate the chemical variables within the system. However, these studies do not include a full evaluation of water stability in NAM or the changing bulk composition of the peridotite due to melt extraction. A coupled approach is necessary to fully address the problem, which includes melting, water in hydrous and nominally anhydrous phases, water-weakening, and a changing bulk composition due to melting.

GyPSM-S (**G**eodynamic and **P**etrological **S**ynthesis **M**odel for **S**ubduction)

(Chapter 2) is used to constrain the development of hydrated regions within the mantle wedge of a subduction zone from a coupled perspective. It involves iterative interaction between ConMan, a two-dimensional thermal and variable viscosity numerical flow model [11], and pHMELTS, a thermodynamic energy minimization algorithm that can calculate water partitioning into NAM [6, 12, 13]. The significance of the coupled scheme is the detailed tracking of fluids and their rheological and chemical effects from release to initiation of melting. The primary results of the GyPSM-S models demonstrate the existence of a low-viscosity channel (LVC) within the mantle wedge, the process by which LVCs form, and the limitations on the LVC geometry (Chapter 2).

The LVC is effectively a zone of water saturation that develops immediately adjacent to the subducting slab and extends into the wedge to variable distances depending on subduction parameters. It consists of hydrous phases and NAM with high water contents (water solubility increases with pressure, and can approach thousands of ppm at the base of the model domain when all NAM phases are considered). The thickness of the zone is limited at the base by the subducting plate and at the top by the spatial position of the water-saturated peridotite solidus within the wedge. Variations in thickness of the LVC from model to model depend on the thermal structure within the wedge and the intensity and location of fluid sources from the slab. Due to assumptions of vertical fluid transport within GyPSM-S, active melting initiates almost directly over fluid sources, and is confined to a relatively thin layer (~6 km) immediately above the LVC. This restriction on the thickness of the melting region is a function of the near-fractional melting scheme employed within GyPSM-S as well as the assumption that water transport can only occur within a hydrous fluid, as opposed to a hydrous migrating melt. As water is partitioned

strongly into the melt phase, once the water-saturated solidus is crossed, the water activity

in the system drops below unity and no water is available for further transport in a hydrous

fluid phase, resulting in the cessation of melting. Seismic tomography has allowed

imaging of inclined low-velocity zones sub-parallel to the slab within the mantle wedge,

coincident with the instantaneous melting regions predicted by GyPSM-S [14]. In

pressure-temperature space, the peridotite solidus is a function of composition. With the

near-fractional melting scheme implemented in pHMELTS, melts are removed above a

certain residual porosity, and therefore the bulk composition of the advecting solids

changes (becoming more depleted in incompatible elements) along with the solidus

temperature.

LVCs exist over a large range of subduction parameter space (slab age,

convergence velocity, slab dip angle) and can be important for considering the initiation of

melting within the wedge, the state of stress within the wedge, and for changing slab dip

angle [15] as well as for transport of hydrated, relatively fertile near-slab material into the

deep mantle [5, 16-20]. The influence of the existence of the LVC and other localized

low-viscosity geometries within the wedge on the overall flow field and force balance can

be examined through surface observations sensitive to the viscosity structure, such as

dynamic topography and gravity and geoid anomalies [21, 22]. The geoid measurement

represents a combination of contributions from internal density variations (thermal and

mineralogical) and from boundary deformations induced by the flow field [23, 24].

Subduction zones can be characterized by having long-wavelength (10^3 - 10^4 km) geoid

highs over slabs and shorter wavelength (10^2 km) geoid lows over trenches [25, 26]. Long-

wavelength geoid highs are interpreted as indicative of a radial viscosity structure where

the viscosity of the upper mantle (η_{UM}) is less than the viscosity of the lower mantle (η_{LM}), leading to regional compensation of subducting slabs [24, 27]. However, shorter-wavelength geoid anomalies and the depth of back-arc basins may be resolved by studying viscosity variations caused by thermal or compositional variations within the upper mantle [26]. Numerical models have demonstrated that stresses are transmitted through viscous coupling in the wedge from the subducting slab to the overlying lithosphere [25, 28, 29]. Billen and Gurnis [21] demonstrated that a localized region of low viscosity within the upper mantle rather than an overall change in asthenospheric viscosity was required to match the topography and geoid signal on the overlying plate, as a reduction in wedge viscosity reduces the coupling between the slab and the overlying plate, resulting in a less negative dynamic topography. Billen and Gurnis [22] then successfully investigated the relative sizes and shapes of low-viscosity, low-density regions necessary to match signals in the Tonga-Kermadec and Central Aleutian subduction zones. While it is thus well understood that localized low-viscosity regions may be important to the force balance within mantle wedges, the mechanisms of development of these regions and how the regional geometries change based on changing subduction behaviors have only recently been established (Chapter 2). The next logical step would be to attempt to match observed geophysical signals in a particular locality with a modeled fluid-source-based hydration structure. Accordingly, in this study, we present the impact of GyPSM-S modeled localized low-viscosity regions on geophysical signals (topography and geoid and gravity anomalies) from the northern Izu-Bonin subduction system (32 ºN latitude, ~136-146 ºE longitude), particularly emphasizing the manner of development of the low-viscosity region as the primary influence on the geometry.

The northern Izu-Bonin (NIB) subduction system can be described by the descent of relatively old (~135 Ma) Pacific lithosphere beneath the younger Philippine Sea Plate at a moderate convergence velocity of around 5.0 cm/yr and a convergence angle of 45º (Fig. 1) [30]. The Izu-Bonin arc crust between the Izu-Ogasawara trench and the Shikoku Basin is relatively thin (~20 km), and is defined by a narrow (~300 km in width) topographic high over the arc of ~3 km with an associated gravity high of ~100 mGal. The trench is defined by a topographic low of ~ -3 km and a gravity low of ~ -280 mGal. Seismic investigation has determined a velocity structure that can be interpreted as different lithological layers within the arc crust [31-34], most notably a middle crustal layer with *P*-wave velocities approximating mean continental crustal velocities (6.4 km/s [35]). To the west of the arc (Shikoku back-arc basin), and to the east of the trench (Pacific plate), the oceanic crust is uniformly ~8 km in thickness [32]. The relative offset in the bathymetry on either side of the arc-trench area is due to the difference in ages of the two converging oceanic plates. The geoid, filtered from degree and order 2 to 70, is described by a broad high over the arc complemented by a low over the trench. The close proximity of the Kyushu trench and arc to the west leads to a somewhat lower amplitude high and a general decrease towards the west. Altogether, the change in height of the geoid is on the order of ~20 meters. Seismicity within the slab extends to depths of ~475 km, and there is seismic evidence for flattening of the slab within the transition zone [36-40].

2. Method

2.1. Initial GyPSM-S calculation of the shallow hydrated wedge

We used the GyPSM-S model (see Chapter 2 for full GyPSM-S model description) to describe the shallow wedge structure (< 200 km depth) for the NIB system (Fig. 2, Tables 1, 2). This allows an investigation of the development of the hydrated region immediately adjacent to the slab, from initiation to a state independent of the initial conditions and the initial fluid transient.

2.2.Extension of model domain for calculation of geophysical signals

Upon obtaining the GyPSM-S result for the shallow mantle wedge for NIB, a separate, uncoupled model for calculation of topography and geoid and gravity anomalies is constructed using ConMan (Fig. 3a) [12]. A penalty formulation is used to enforce incompressibility in the solution of the momentum equation [12]. The dynamics are controlled by conservation equations of mass, momentum, and energy with the Boussinesq approximation. The non-dimensional equations for mass and momentum are:

$$\nabla \cdot v' = 0 \qquad \text{and} \qquad (1)$$

$$\nabla P' - \nabla \cdot \left(\eta' \nabla v' \right) = Ra T' \hat{k} \qquad , \qquad (2)$$

where v' is the dimensionless velocity, T' is the dimensionless temperature, P' is the dimensionless pressure, η' is dimensionless viscosity, and $\hat{k}$ is a unit vector in the direction of gravity. The dimensionless Rayleigh number combines all the material properties:

$$Ra = \frac{g\alpha\rho\Delta T d^3}{\kappa\eta} \quad , \tag{3}$$

where g is the acceleration due to gravity, α is the coefficient of thermal expansion, ΔT is the temperature drop across the box, d is the depth of the box, κ is the thermal diffusivity, and η is the dynamic viscosity (Table 1). The non-dimensional energy equation is:

$$\frac{\partial T'}{\partial t'} = -v' \cdot \nabla T' + \nabla^2 T' \quad , \tag{4}$$

where t' is dimensionless time. A streamline upwind Petrov-Galerkin method [43] is used to solve Eq. (4). The model domain was extended vertically and horizontally in order to account for the long-wavelength features in the geoid signal. The model domain, 9000 km in width, extends from the surface to the core-mantle boundary (3000 km). The refined computational grid consists of 45000 bilinear quadrilateral elements: 150 in the vertical direction and 300 in the horizontal, and element resolution ranges from (40 km × 40 km) to (10 km × 10 km). A refined zone that includes the GyPSM-S subdomain has the highest resolution (10 km × 10 km). We do not explicitly include a fault. The initial thermal structures of the subducting slab and of the overlying lithosphere are defined by a half-space cooling model for each plate based on age, and the top and bottom surfaces of the model domain have isothermal, no-slip boundary conditions. The wedge flow field consists of analytical corner flow [44], and the thermal structure for the wedge is determined by solving the advection-diffusion equation (Eq. 4) with the fixed flow field to

steady-state. Instantaneous flow is driven by internal thermal and chemical buoyancy forces. The slab contributes the primary thermal variation. Imposed chemical heterogeneities such as crustal layering, mineralogical phase transformations, and variations in the degree of wedge hydration are introduced as density variations and represent sources of buoyancy. The slab velocities are kinematically imposed, and slab dip in the upper mantle is a constant 45º, with a flattening to near-horizontal within the transition zone.

2.3. Internal density variations and background radial viscosity

The area of interest is restricted to the Izu-Ogasawara trench, the arc edifice, and oceanic crust immediately to the west and east (~136-146 ºE longitude). We do not account for additional structures further to the west and east in the extended model domain. A lower density island arc could contribute to topographic and gravity highs [28, 55]. Therefore, we include low-density crustal layering in the models. Arc crustal structure is defined by density anomalies interpreted from seismic velocities from the Shikoku Basin to the Izu-Ogasawara Trench [31, 32]. The along-arc variation of the crustal structure in the NIB system is distinguished by the presence of three layers: (i) upper crust interpreted as sediments and basalts with velocities that increase with depth from 1.5 km/s to 5.6 km/s over 5 km, (ii) middle crust with *P*-wave velocities of 6.1-6.3 km/s, corresponding to intermediate (andesitic to tonalitic) plutonic rocks that are close to the mean velocity of continental crust (~6.4 km/s [35]), and (iii) thick lower crust with *P*-wave velocities of 7.1-7.3 km/s, interpreted to be gabbroic igneous underplating [32]. The arc crustal thickness

varies from 18 km below the forearc to 20 km beneath the central rift zone 260 km from the trench [32].

The crustal structure of the subducting Pacific plate is ~8 km thick and can be subdivided into three layers: (i) an upper crustal layer with two defining velocity characteristics: upper layer with *P*-wave velocities ranging from 1.6-1.8 km/s, and a lower layer with velocities of 3.0-4.3 km/s, (ii) middle layer with velocities of 4.7-5.7 km/s, and (iii) a lower layer with velocities 6.4-6.5 km/s [32]. For simplicity, we assume that the crust of the Shikoku Basin is the same as the Pacific plate. We are somewhat limited by the resolution of the model (10 km vertical increments along the topmost elements) in re-constructing a realistic density structure within the crust, however, we attempt to include the most important density variations despite the restrictions in resolution.

The exothermic phase transformation from olivine to wadsleyite ($\alpha \rightarrow \beta$) is represented by a density increase of 7.2% at 410 km depth, and the endothermic phase transformation from ringwoodite (γ) to perovskite plus magnesiowüstite is represented by a density increase of 8.4% at 670 km depth [50], with deflections above and below these depths associated with the cold subducting slab. The basalt to eclogite transition within the slab is accounted for by a 6% density increase within the altered oceanic crustal (AOC) layer of the down going plate. Despite evidence that including the effects of phase transformations near the transition zone in the calculation of the dynamic topography and the geoid is insignificant considering the overwhelming effect of the radial viscosity structure [51], we include these effects as part of a comprehensive approach.

The radial background viscosity structure consists of several layers: lithosphere, upper mantle, transition zone, and lower mantle. Viscosity is both temperature- and

composition-dependent, with the viscosity in each layer defined with respect to a reference

viscosity (η_0) with a value of 3.0×10^{20} Pa s: upper mantle ($\eta_{UM} = 1 \times \eta_0$), transition zone ($\eta_{TZ}$

$= 100 \times \eta_0$), lower mantle ($\eta_{LM} = 300 \times \eta_0$), and lithosphere ($\eta_{LITH} < 100$ km depth, $1000 \times \eta_0$).

The maximum viscosity of the slab at all depths is $1000 \times \eta_0$. Parameterized regions (Fig.

3b) of hydration within the upper mantle are included based on output from the GyPSM-S

model, where reductions in viscosity within the hydration zones are due to higher

concentrations of water in NAM and the superposition of the thermal structure in the

wedge. A depth of 400 km is considered a probable maximum for the parameterized

hydrated regions in this system because of the flattening of the slab in the transition zone.

2.4.Calculation of geophysical surface observables

Calculated topography (*h*), geoid height (*ΔN*), and gravity anomalies (*Δg*) are

compared with observations to assess the appropriateness of the viscosity and buoyancy

models. We evaluate not only the preferred parameterization, which includes an extended

LVC region (ELVC), but also other models (no LV region, uniform thickness LVC, and

LVW) (Fig. 4). We additionally evaluate the impact of different degrees of hydration of

the low-viscosity zone, leading to different magnitudes of lateral viscosity contrast within

the wedge, and we evaluate different magnitudes of density contrast between the hydrated

zones and the ambient nominally anhydrous wedge. The treatment in the GyPSM-S model

is to use water content in olivine as the sole compositional influence on the viscosity law:

$$\eta' = \frac{\eta}{\eta_0} = \exp\left[\left(\frac{Q}{RT_0}\right) * \left(\left(\frac{T_0}{T}\right) - 1\right)\right] * \left(\frac{XH_2O}{XH_2O_{crit}}\right)^{-1} \quad , \qquad (5)$$

where $XH_2O > XH_2O_{crit}$, η_0 is the reference viscosity, Q is the activation energy, R is the gas constant, T_0 is the model reference temperature, XH_2O is the water content in olivine, and XH_2O_{crit} is the critical value for water weakening (Table 1). At upper mantle pressures and temperatures, olivine is the dominant mineral in the solid matrix, and experimental studies have focused on dislocation creep in hydrated olivine aggregates as a mantle proxy [8, 45]. However, substantial amounts of water can also go into other NAM, such as the pyroxenes and garnet.

The dynamic topography (h) balances the the normal stress on the top surface and becomes:

$$h = \frac{\eta_0 \kappa}{\Delta\rho \, gd^2} \sigma'_z \qquad , \qquad (6)$$

where σ'_z is the non-dimensional stress, $\Delta\rho$ is the density difference across the top of the domain (representing the contrast between lithosphere and water, as we assume the top surface of the domain is covered by water), and d is the depth of the model domain (Table 1). We calculate topography using the consistent boundary flux (CBF) method [46]. We match our model topography results with the residual topography, which is the topography that results when the normal subsidence of the oceanic lithosphere is removed from the observed bathymetry (Fig. 1), using:

$$h_T = h_0 - (2600 + 220 \, (A)^{\frac{1}{2}}) \qquad , \qquad (7)$$

where h_T is the residual depth in meters, A is the age of the oceanic lithosphere in Myr (Table 1), and h_0 is the observed bathymetry in meters [47, 48]. We compute the predicted geoid height in the wavenumber domain and include contributions from topography on the top surface and density anomalies within the model domain, assuming no density anomalies outside the domain (density anomalies within the domain are converted into mass sheets at each layer of nodes within the model, and topography along the top surface is likewise converted to a mass sheet and summed to form the surface response). To account for the difference in model plate ages, the topography is shifted by a mean value along the edge of the domain before computing geoid height. Testing of the topography and geoid calculations against established benchmarks [49] was performed (Appendix IV-A). Gravity anomalies are also computed in the wavenumber domain. The gravity and geoid results were both subjected to low bandpass filters in order to attenuate frequencies higher than were represented in the regional datasets.

3. Modeling Results

3.1. GyPSM-S modeling of NIB shallow wedge structure

The NIB model results (Fig. 2) show the development of the hydrated wedge due to the subduction of a mature slab at a moderately slow convergence velocity (Chapters 2, 3).

The locations of the dehydration reactions within the slab layers are determined by the relatively cool thermal structure and result in a bimodal distribution. Low- to mid-pressure fluid releases are dominantly from the AOC layers (from increasing depths into the slab), and strong, high-pressure fluid release originates in the lithospheric serpentinite slab layer. The fluid release from the serpentinite layer results in a continuous cooling of the melting region, due to the effects of latent heat of melting. This cooling culminates in a retreat of the water-saturated solidus into the wedge, and a lengthening of the deeply-originating fluid transport pathway, leading to the development of a long hydration corridor through the wedge. Ultimately, with advection of this hydrated region by corner flow towards the slab, the shallow hydrated region approaches the shape of a wedge (LVW), or a very thick channel (ELVC), where the left boundary of the hydrated geometry is controlled by the deepest location of fluid release from the slab, assuming a vertical fluid trajectory. The higher-pressure extension of the ELVC is in the form of a uniformly-thick LVC, as the flow field continues along near-slab-parallel streamlines. This particular shape is in contrast to the relatively uniformly thick low-viscosity channels (LVC) associated with the subduction of relatively younger slabs, or when the slab dip angle is steeper, resulting in narrowing of the region of fluid infiltration into the wedge.

Through water-weakening, these regions of water-saturation translate into low-viscosity zones relative to the ambient solid matrix. In this end-member case of vertical fluid transport, it is the interplay between the slab dip angle and the deepest location of slab fluid release that determines the lateral extent of the wedge geometry. The depth extent of the GyPSM-S model is controlled by the stability of pHMELTS (< 200 km). However, there is evidence for the deeper stability of hydrous phases, such as phase-A, which may

result in deeper fluid releases and a wider wedge geometry (LVW). The hydrated NAM, as opposed to hydrous mineral phases, are stable, and can transport water to great depths (Chapter 2), the basis for the theoretical continuation of the LVC to the transition zone. We investigate the response of surface observables for several geometries of varying upper mantle lateral viscosity (no LV, LVC, ELVC, and LVW) (Table 3).

As a result of the viscosity formulation (Eq. 5), the viscosity calculated is a function of both temperature and composition, specifically, water content in olivine. Therefore, the viscosity within the hydrated regions (parameterized by an average $XH_2O_{olivine}$), while significantly reduced relative to an anhydrous value, is non-uniform due to the superimposed thermal structure. Density variations produced by the GyPSM-S calculation for the low-viscosity regions relative to ambient nominally anhydrous mantle wedge are on the order of $\Delta\rho \sim$ -50 to -20 kg/m^3. However, previous modeling [22] investigated the range $\Delta\rho \sim$ -50 to 0 kg/m^3, and we therefore include this range in the geophysical modeling for completeness (Table 3). The low-viscosity regions calculated by GyPSM-S effectively increase the upward component of flow as material crosses the boundary between the nominally anhydrous mantle wedge and the hydrated region.

3.2. Topography

Incorporation of the low-viscosity region has the primary influence of increasing the topography associated with the arc edifice. Without a low-viscosity region (no LV, Fig. 5e), the calculated topography for the arc is too low and too narrow as compared with that observed, and the trench depth is underestimated. When a low-viscosity channel is

added (LVC1, Fig. 5f), fore-arc topography increases to more closely match that observed and trench depth increases to match that observed. The incorporation of the wedge-type structure (ELVC4, Fig. 5g) generates a peak in the arc topography associated with the maximum horizontal extent of the hydrated region in the shallow mantle wedge, more closely matching the amplitude of the observed dataset in that area. Increasing the relative viscosity difference between the ambient mantle wedge and the low-viscosity region by increasing the amount of water in olivine (ELVC5) results in a further increase in the calculated topography by 280 m and an increase in the trench depth.

Increasing the lateral and depth extent of the ELVC to approach a true wedge (LVW2, Fig. 5h) has a significant influence on the shape of the calculated topography. The lateral extent of the ELVC/LVW corresponds to the deepest point of slab dehydration, assumed to result in a long fluid pathway similar to the NIB GyPSM-S model result (Chapter 2, Fig. 2). As the lateral extent of the ELVC increases from the nominal LVC width (50 km), the topography changes from a smooth top to one that peaks within the arc, followed by the smooth top again as the increases in calculated topography due to the low-viscosity zone are added away from the highs associated with the arc edifice (Fig. 6a). The peak is caused by the sharp edge to the low-viscosity region that results in a concentration in stress [26]. Therefore, the peaks in the topography over the relatively narrow (~300 km) Izu-Bonin arc edifice require a low-viscosity region directly beneath it. Because the maximum width LVW (LVW2, 400 km) does not result in a peaked signal, this calculation cannot constrain a maximum depth of fluid release. However, the calculation can be very useful in determining shallower depths of fluid release from the slab, most likely between 100 and 250 km depth and involving dehydration of a lithospheric serpentinite slab source.

Adding, and then changing, the shape of the low-viscosity region (LVC to ELVC) increases trench depth, and more closely predicts of the trench depth compared with that observed. Changing the density within the low-viscosity regions to match GyPSM-S output has an additional significant effect on the calculated topography (Fig. 6b, c). Decreasing the density in the ELVC due to water-saturation by 20 kg/m^3 (the lower end of the value predicted by GyPSM-S modeling) relative to the ambient nominally anhydrous wedge results in a very close match of the calculated topography and that observed by increasing both the maximum height of the model topography (by ~2.3 km) and the width of the model topography. Decreasing the density by the maximum value (50 kg/m^3) results in a considerable over prediction of topographic height (by ~3.4 km). Based on the calculated topography, the preferred parameters, which result in a close match to the amplitude and width of the regional dataset as judged by the NRMS deviation (Fig. 7a), involve the horizontal extension of the shallow wedge hydration region to ~200-350 km and include a density contrast within the LV zone of -30 to -10 kg/m^3, which is on the lower end of the range predicted by [22].

3.3. Gravity anomalies and geoid height

Prediction of the gravity associated with the Izu-Bonin trench and arc system, but with no low-viscosity region, results in a slight under prediction of trench depth and near-trench variations (Fig. 5i). Similar to the results for topography, introduction of an LVC produces a larger amplitude high near the trench, providing a better match to that observed (LVC1, Fig. 5j), particularly in the fore-arc region. Lateral extension of the LVC in the

shallow wedge results in an increasing amplitude for the gravity anomaly away from the trench, and significant over predictions relative to the regional dataset (Fig. 5k, Fig. 6d). However, extension of the low-viscosity region into an LVW geometry, where hydration is produced at depths beyond the arc edifice, provides a better match to that observed (LVW2, Fig. 5l).

Introducing a density variation within the modeled low-viscosity regions results in a similar effect as in the topography, specifically an increase in amplitude (Fig. 6e, f). As the topography in the arc region increases, due to a lessening of the dynamic depression of the arc, the gravity anomaly increases. Varying the density contrast from -50 to 0 kg/m^3 between the low-viscosity region and the ambient mantle wedge in conjunction with the lateral extent of the LV zone shows that the best fit to the regional gravity profile is actually given by $\Delta\rho$ = -10 to 0 kg/m^3 over a range of lateral extents, or an LVC geometry with $\Delta\rho$ = -30 to 0 kg/m^3 (Fig. 7b).

Calculation of the model geoid height without a low-viscosity region results in a broad high over the arc and a broad low over the trench, with a similar shape to the observed dataset (Fig. 5a). The amplitude for the height over both the arc and the trench is larger than that of the regional dataset. Addition of a low-viscosity region increases the amplitude over the arc (Fig. 5b-d), and increasing the relative viscosity contrast by increasing the average water in olivine content has no apparent effect. In fact, besides the initial perturbation seen with the introduction of the LVC from the case lacking any low-viscosity zone, changing geometry of the low-viscosity region does not have a significant effect on the geoid height.

4. Discussion

4.1.Subduction parameters and LV zone geometry

It is apparent from the modeling results in this, and previous [21, 22, 26], studies that the particular geometry of the localized low-viscosity zone is important, and can be reflected in surface observations of geophysical quantities over subduction zones. Previous investigations have alluded to the role of fluids in producing the low-viscosity region, and have imposed specific geometries to match regional observations of the dynamic topography, geoid and gravity anomalies [22]. However, this study is based on the results from coupled geochemical and geodynamic modeling that tracks fluids from sources within the slab through reaction of the fluids with the slab-adjacent wedge material to melt production, resulting in the development of hydrated regions within the wedge (Chapter 2). Variations in the geometry of the hydrated regions result from changing subduction parameters such as slab dip, convergence velocity, and slab age and the time-dependence of the hydration process. We therefore are able to link fundamental aspects in subduction zones such as the depth of fluid transport within the slab, the dehydration pattern, fluid flux, and fluid migration pathways with the resulting size and depth extent of low-viscosity regions within the wedge. This study compares the results of modeling a particular subduction region (NIB) to surface observations of topography, gravity and geoid anomalies, to test the ability of the coupled model to determine the low-viscosity geometry.

The primary influence on the geometry of the LVC are the fluid release pattern

from the slab, which, in turn, depends on the thermal structure of the slab mostly

determined by slab age, and the slab dip, as steeper-dipping slabs lead to narrower regions

of fluid infiltration. Slab convergence velocity has a secondary influence on fluid release

pattern and is therefore a second-order control on LVC geometry. More mature slabs, such

as seen in the NIB model, allow for shallower fluid releases from the AOC layers within

the slab, and a strong, deep fluid release from the serpentinite layer within the slab. The

strong, deep fluid release may result in the time-dependent lengthening of the deep fluid

pathway, and an eventual ELVC structure. Limitations on the depth extent of the GyPSM-

S model domain restrict modeled dehydration to less than 200 km, but it is possible for

even deeper dehydration reactions to occur either within the slab serpentinite layer or

within hydrous phases stabilized within the hydrated slab-adjacent wedge. Assuming a

similar lengthening of the fluid pathways, LVW structures with a greater lateral extent may

form from even deeper slab fluid sources. In NIB, however, comparison of the observed

topography and gravity signals with computed values results in the conclusion that fluid

release occurs within the interval 150-350 km depth, with an associated density reduction

within the LV zone of $\sim$ -10 kg/m^3 (Fig. 7c), values in agreement with GyPSM-S results.

Subduction of younger slabs results in a fluid release pattern involving low- to mid-

pressure dehydration of the AOC layers and the serpentinite layers within the slab, and a

deep release from the serpentinite layer. However, due to the warmer thermal structure,

the deepest reaction does not produce a similar intensity of fluid release as in the mature

slab case, and the hydration structure is of approximately uniform thickness to the base of

the model domain (LVC), with slight thickening directly over locations of fluid infiltration.

Changing slab dip does not appear to impact the dehydration pattern, but does influence the

geometry of the low-viscosity region generated.

The results of this study were influenced by the inclusion of the high-viscosity lid, background radial viscosity structure, low-density crustal model, and the higher-density eclogite layer within the slab, but not by the inclusion of the phase transformations associated with transition zone seismological boundaries. The background values for the transition zone and lower mantle viscosity ($100 \times \eta_0$, $300 \times \eta_0$) are relatively high, compared with previous studies [24].

For this study, we imposed an uniform, average value for water content in olivine over the entire low-viscosity region of either 1000 ppm (model ELVC4) or 2000 ppm (model ELVC5). GyPSM-S calculated water contents in olivine over the shallow water-saturated wedge (< 200 km depth) for the NIB model range from 150 - 1400 ppm, increasing with pressure, and so this average value does not reflect the more complex hydration structure of the wedge and may have an impact on the results. The basis for the compositional part of the viscosity law (Eq. 5) is water in olivine, based on experimental results involving dislocation creep in olivine, and on the assumption of an olivine-dominated rheology, which is appropriate for the mantle. However, a significant fraction of the mantle includes other nominally anhydrous minerals which can accommodate high water contents (clinopyroxene: 600-3000 ppm H_2O). Additional water-weakening due to these minerals may be a factor as well, making the high modeled water contents in the shallow wedge not as extreme. Assuming a peridotite assemblage of 57% olivine, 8% garnet, 16% orthopyroxene, and 16% clinopyroxene, the LVC can potentially hold ~2200 ppm H_2O at the base of the GyPSM-S model domain (200 km). We observe a significant influence on the topography with decreasing viscosity within the hydrated zones caused by

increasing average water contents in olivine.

4.2.Comparison with previous regional models of low-viscosity zones

Billen and Gurnis [22] modeled potential low-viscosity, low-density zones corresponding to two model regions (Tonga-Kermadec and Central Aleutians) with differing subduction parameters. However, the mechanism by which such a zone would form was not directly addressed, and the ultimate geometry of the low-viscosity region was inferred by comparison of regional datasets with computed values for topography and geoid height. Results indicated that both subduction wedges included low-viscosity, low-density regions, but the the size of the region and magnitude of the density anomaly within the Tonga-Kermadec subduction zone was greater than that for the Central Aleutians. The primary difference between the two subduction zones is the age of the subducting slab. Tonga-Kermadec involves an older slab (~105 Ma), while the Central Aleutians involves a significantly younger slab (~55 Ma) [52]. Calculations made by [52] of the depth of the slab beneath the volcanic front (H') may indicate that the Central Aleutians may involve shallower fluid release (and melting) than Tonga-Kermadec, with H' of ~90 km and ~115 km, respectively. GyPSM-S modeling indicates that subduction of a more mature slab results in deeper fluid releases, and the possibility for the development of a larger low-viscosity region, in agreement with the results from [22].

5. Conclusions

Inclusion of a localized low-viscosity, low-density zone in subduction zone modeling is required in order to match geophysical surface observations. Coupled geochemical and geophysical modeling (GyPSM-S) allows for a fluid-source-based approach to determining a particular low-viscosity geometry based on changing subduction parameters, spatial location of the water-saturated solidus, and the water contents of nominally anhydrous minerals. Subsequent modeling of the topography and gravity and geoid anomalies with inclusion of the particular low-viscosity geometry can then be performed and compared with observed values. For the NIB system, comparison of the observed topography signal with computed values results in the conclusion that fluid release occurs within the interval ~150-350 km depth, forming an extended low-viscosity zone (ELVC) with an associated density reduction within the ELVC of ~ -10 kg/m^3, values in general agreement with GyPSM-S results emphasizing deep dehydration from subducting lithospheric serpentinite.

Acknowledgments

References

[1] D. R. Bell and G. R. Rossman (1992) Water in Earth's mantle: the role of nominally anhydrous minerals. Science **255** (5050), 1391-1397.

[2] J. H. Davies and D. J. Stevenson (1991) Physical model of source region of subduction zone volcanics. Journal of Geophysical Research **97**(B2), 2037-2070.

[3] T. L. Grove et al. (2006) The influence of H_2O on mantle wedge melting. Earth and Planetary Science Letters **249**, 74-89.

[4] H. Iwamori (1998) Transportation of H_2O and melting in subduction zones. Earth and Planetary Science Letters **160**, 65-80.

[5] H. Kawakatsu and S. Watada (2007) Seismic evidence for Deep-Water Transportation in the Mantle. Science **316**, 1468-1471.

[6] P. D. Asimow, J. E. Dixon, C. H. Langmuir (2004) A hydrous melting and fractionation model for mid-ocean ridge basalts: Application to the Mid-Atlantic Ridge near the Azores. Geochemistry, Geophysics, Geosystems **5**(1), Q01E16, doi:10.1029/2003GC000568.

[7] G. A. Gaetani and T. L. Grove (2003) Experimental constraints on melt generation in the mantle wedge. Geophysical Monograph **138**, 107-134.

[8] G. Hirth and D. L. Kohlstedt (1996) Water in the oceanic upper mantle; implications for rheology, melt extraction, and the evolution of the lithosphere. Earth and Planetary Science Letters **144** (1-2), 93-108.

[9] D. Arcay et al. (2005) Numerical simulations of subduction zones: Effect of slab dehydration in the mantle wedge dynamics. Physics of the Earth and Planetary Interiors **149**, 133-153.

[10] T. V. Gerya and D. A. Yuen (2003) Rayleigh-Taylor instabilities from hydration and

melting propel 'cold plumes' at subduction zones. Earth and Planetary Science Letters **212**, 47-62.

[11] S. King et al. (1990) ConMan; vectorizing a finite element code for incompressible two-dimensional convection in the Earth's mantle. Physics of the Earth and Planetary Interiors **59**(3), 195-207.

[12] P. M. Smith and P. D. Asimow (2005) Adiabat_1ph: A new public front-end to the MELTS, pMELTS, and pHMELTS models. Geochemistry, Geophysics, Geosystems **6**(2), Q02004, doi:10.1029/2004GC000816.

[13] M. S. Ghiorso and R. O. Sack (1995) Chemical mass transfer in magmatic processes; IV, A revised and internally-consistent thermodynamic model for the interpolation and extrapolation of liquid-solid equilibrium magmatic systems at elevated temperatures and pressures. Contributions to Mineralogy and Petrology **119**(2-3), 197-212.

[14] A. Hasegawa et al. (2005) Deep structure of the northeastern Japan arc and its implications for crustal deformation and shallow seismic activity. Tectonophysics **403**, 59-75.

[15] V. Manea and M. Gurnis (2007) Subduction zone evolution and low viscosity wedges and channels. Earth and Planetary Science Letters **264**(1-2), 22-45.

[16] M.W. Schmidt and S. Poli (1998) Experimentally based water budgets for dehydrating slabs and consequences for arc magma generation. Earth and Planetary Science Letters **163**, 361– 379.

[17] K. M. Cooper et al. (2004) Oxygen isotope evidence for the origin of enriched mantle beneath the mid-Atlantic ridge. Earth and Planetary Science Letters **220**, 297-316.

[18] K. E. Donnelly et al. (2004) Origin of enriched ocean ridge basalts and implications for mantle dynamics. Earth and Planetary Science Letters **226**, 347-366.

[19] J. E. Dixon et al. (2002) Recycled dehydrated lithosphere observed in plume-influenced mid-ocean-ridge basalt. Nature **420**, 385-389.

[20] P. J. le Roux et al. (2002) Mantle heterogeneity beneath the southern Mid-Atlantic Ridge: trace element evidence for contamination of ambient asthenospheric mantle. Earth and Planetary Science Letters **203**, 479-498.

[21] M. I. Billen and M. Gurnis (2001) A low viscosity wedge in subduction zones. Earth and Planetary Science Letters **193**, 227-236.

[22] M. I. Billen and M. Gurnis (2003) Comparison of dynamic flow models for the Central Aleutian and Tonga-Kermadec subduction zones. Geochemistry, Geophysics, Geosystems **4**(4), 1035, doi:10.1029/2001GC000295.

[23] G. F. Davies (1981) Regional compensation of subducted lithosphere: effects on geoid, gravity and topography from a preliminary model. Earth and Planetary Science Letters **54**, 431-441.

[24] B. H. Hager (1984) Subducted slabs and the geoid: Constraints on mantle rheology and flow. Journal of Geophysical Research **89**(B7), 6003-6015.

[25] S. Zhong and M. Gurnis (1992) Viscous flow model of a subduction zone with a faulted lithosphere: Long and short wavelength topography, gravity and geoid. Geophysical Research Letters **19**(18), 1891-1894.

[26] M. I. Billen et al. (2003) Multiscale dynamics of the Tonga-Kermadec subduction zone. Geophysical Journal International **153**, 359-388.

[27] L. Moresi and M. Gurnis (1996) Constraints of the lateral strength of slabs from three-

dimensional dynamic flow models. Earth and Planetary Science Letters **138**, 15-28.

[28] N. H. Sleep (1975) Stress and flow beneath island arcs. Geophysical Journal International **42**, 827-857.

[29] S. Zhong et al. (1998) Role of faults, nonlinear rheology, and viscosity structure in generating plates from instantaneous mantle flow models. Journal of Geophysical Research **103**(B7), 15255-15268.

[30] R. J. Stern et al. (2003) An Overview of the Izu-Bonin-Mariana Subduction Factory. Geophysical Monograph 138, 175-222.

[31] K. Suyehiro et al. (1996) Continental crust, crustal underplating, and low-Q upper mantle beneath an oceanic island arc. Science **272**, 390-392.

[32] N. Takahashi et al. (1998) Implications from the seismic crustal structure of the northern Izu-Bonin arc. The Island Arc **7**, 383-394.

[33] N. Takahashi et al. (2007) Crustal structure and evolution of the Mariana intra-oceanic island arc. Geology **35**(3), 203-206.

[34] K. Kitamura et al. (2003) Petrological model of the northern Izu-Bonin-Mariana arc crust: constraints from high-pressure measurements of elastic wave velocities of the Tanzawa plutonic rocks, central Japan. Tectonophysics **371**, 213-221.

[35] N. I. Christensen and W. D. Mooney (1995) Seismic velocity structure and composition of the continental crust: A global view. Journal of Geophysical Research **100**, 9761-9788, doi: 10.1029/95JB00259.

[36] R. Van der Hilst et al. (1991) Tomographic imaging of subducted lithosphere below northwest Pacific island arcs. Nature **353**, 37-43.

[37] Y. Fukao et al. (1992) Subducting slabs stagnant in the mantle transition zone.

Journal of Geophysical Research **97**, 4809-4822.

[38] S. Widiyantoro et al. (1999) Seismic tomography with P and S data reveals lateral variations in the rigidity of deep slabs. Earth and Planetary Science Letters **173**(1-2), 91-100.

[39] Y. Fukao et al. (2001) Stagnant slabs in the upper and lower mantle transition region. Reviews of Geophysics **39**(3), 291-323.

[40] A. Gorbatov and B. L. N. Kennett (2003) Joint bulk-sound and shear tomography for Western Pacific subduction zones. Earth and Planetary Science Letters **210**, 527-543.

[41] D. T. Sandwell and W. H. F. Smith (1997) Marine Gravity from Geosat and ERS-1 Altimetry. Journal of Geophysical Research **102**, 10039-10054.

[42] F. G. Lemoine et al. (1998) The Development of the Joint NASA GSFC and NIMA Geopotential Model EGM96. NASA Goddard Space Flight Center, Greenbelt, Maryland, 20771 USA.

[43] A. N. Brooks and T. J. R. Hughes (1982) Streamline Upwind Petrov-Galerkin Formulations for Convection Dominated Flows with Particular Emphasis on the Incompressible Navier-Stokes Equations. Computer Methods in Applied Mechanics and Engineering **32**(1-3), 199-259.

[44] G. K. Batchelor (1967) An Introduction to Fluid Dynamics. Cambridge University Press.

[45] G. Hirth and D. Kohlstedt (2003) Rheology of the Upper Mantle and the Mantle Wedge: A View from the Experimentalists. Geophysical Monograph 138, 83-105.

[46] S. Zhong et al. (1993) Accurate determination of surface normal stress in viscous flow

from a consistent boundary flux method. Physics of the Earth and Planetary Interiors **78**, 1-8.

[47] F. Pribac (1991) PhD thesis: Superswells due to mantle convection. Australia National University.

[48] W. Schroeder (1984) The empirical age-depth relation and depth anomalies in the Pacific Ocean Basin. Journal of Geophysical Research **89**, 9873-9883.

[49] B. Blankenbach et al. (1989) A benchmark comparison for mantle convection codes. Geophysical Journal International **98**, 23-38.

[50] R. Jeanloz (1989) High pressure chemistry of the Earth's mantle and core, in Mantle Convection, edited by W. R. Peltier, Pergamon, New York, 203-260.

[51] S. D. King (2002) Geoid and topography over subduction zones: The effect of phase transformations. Journal of Geophysical Research **107**(0), doi: 10.1029/2000JB000141.

[52] E. M. Syracuse and G. A. Abers (2006) Global compilation of variations in slab depth beneath arc volcanoes and implications. Geochemistry, Geophysics, Geosystems **7** (5), Q05017, doi: 10.1029/2005GC001045.

[53] R. D. Müller et al. (1997) Digital isochrons of the world's ocean floor. Journal of Geophysical Research **102**(B2), 3211-3214.

[54] R. Arko et al. (2007) The Global Multi-Resolution Topography (GMRT) Synthesis. EOS Trans. AGU, **88**(52), Fall Meet. Suppl. Abstract IN51B-0405.

[55] S. Zhong and M. Gurnis (1994) Controls on trench topography from dynamic models of subducted slabs. Journal of Geophysical Research **99**(B8), 15,683-15,695.

Figure Captions

Figure 1: (a) Observed free air gravity for the northern Izu-Bonin region [41]; (b) Geoid east-west profile extracted from EGM96 dataset [42] using terms from degree and order 2 to 70 (note that the *x*-scale extends from 120 ºE to 150 ºE to show long-wavelength features); (c) East-west bathymetric profile extracted from the GMRT dataset [54] across 32 ºN, and does not vary appreciably from actual bathymetry; (d) Free air gravity anomaly east-west profile extracted from dataset of [41] (version 15.1).

Figure 2: GyPSM-S results for the viscosity structure of the shallow (< 200 km) mantle wedge for the NIB model calculation showing the influence of the high water contents in NAM as a localized zone of viscosity reduction. The geometry of the low-viscosity region is directly influenced by the vertical migration of water from the dehydrating subducting slab (shown as blue lines), the majority of which is released at depths ≥ 150 km from the lithospheric serpentinite layer.

Figure 3: Uncoupled model setup for calculation of topography, geoid height, and gravity anomalies: (a) schematic representation of calculation domain; (b) schematic representation of model geometries in association with fluid release locations.

Figure 4: Model viscosity structure with addition of parameterized low-viscosity regions: (a) no LV, corresponds to a lack of an imposed low-viscosity zone; (b) LVC, corresponds to a slab-adjacent uniform 50 km thick low-viscosity channel that extends to the top of the

transition zone, or where the slab begins to flatten (note change in viscosity scale); (c) ELVC, corresponds to an "extended" LVC approximating a wedge geometry in the shallow regions of the mantle wedge, but remaining a uniform channel as greater depths due to the near slab-parallel flow field, and (d) LVW, corresponding to a full "wedge"-type geometry.

Figure 5: Results of NIB model calculations (Table 3) for geoid height, gravity anomaly, and topography (thick black lines) compared with regional dataset profiles (thin gray lines) for (a, e, i) no LV; (b, f, j) LVC1 with 1000 ppm H_2O in olivine as an average value; (c, g, k) ELVC4 with 1000 ppm H_2O in olivine as an average value ($\eta_{LV} = 3.3 \times 10^{19}$-$4.0 \times 10^{20}$ Pa s); (d, h, l) LVW2 with 1000 ppm H_2O in olivine as an average value. Note that all models shown have zero density contrast between the LV region and the nominally anhydrous mantle wedge.

Figure 6: Independently varying model parameters. (a, d, b, e) Different lateral extents of models for the ELVC/LVW, corresponding to the depth of fluid release from the slab: (a, d) ELVC1: 100 km extent (black), ELVC2: 150 km extent (red), and ELVC24: 250 km extent (blue), all models having $\Delta\rho = 0$ kg/m^3 between the LV region and the nominally anhydrous mantle wedge and arrows indicating the changing peak position in the calculated topography; (b, e) ELVC9: 100 km extent (blue), ELVC12: 150 km extent (red), and ELVC25: 250 km extent (black), all models having $\Delta\rho = -10$ kg/m^3 between the LV region and the nominally anhydrous mantle wedge. (c, f) Different density contrast between the ambient nominally anhydrous wedge and the ELVC region on calculated topography and gravity anomalies: (c, f) ELVC24: $\Delta\rho = 0$ kg/m^3 (blue), ELVC25: $\Delta\rho = -10$ kg/m^3 (red),

and ELVC26: $\Delta\rho$ = -20 kg/m³ (black), all models having a lateral LV extent of 250 km. The observed profiles are indicated by thinner gray lines in all panels.

Figure 7: Comparison of the result of variation of parameters, specifically the density contrast between the LV zone and the nominally anhydrous mantle wedge and the lateral extent of the LV zone, to the regional profiles for gravity anomalies and topography using RMS error estimates to establish goodness of fit (where darker colors indicate a better fit): (a) normalized RMS error calculated for misfit of calculated topography to that observed; (b) normalized RMS error calculated for misfit of calculated gravity to that observed; and (c) combined normalized RMS error calculated for the misfit of both gravity and topography where dotted lines indicate transects in Fig. 6.

Appendix IV-A: Benchmarking

We applied benchmarking to compare the results for surface observables (topography, geoid) that were produced by this code (ConMan plus Fourier transform analysis). Using Blakenbach et al. [49] cases 1a-c, we put together four models with varying grid resolution and Rayleigh number (Table 4). All models represent a single convection cell with constant viscosity in a square domain. The non-dimensional temperature is fixed to zero at the top and to $\Delta T = 1.0$ at the base. There is reflecting symmetry at the sidewalls and zero shear stress along all boundaries [49]. The benchmarking exercise was successful in reproducing published results.
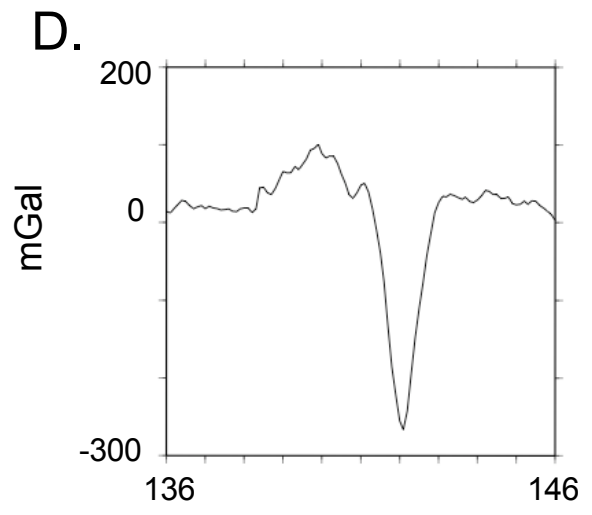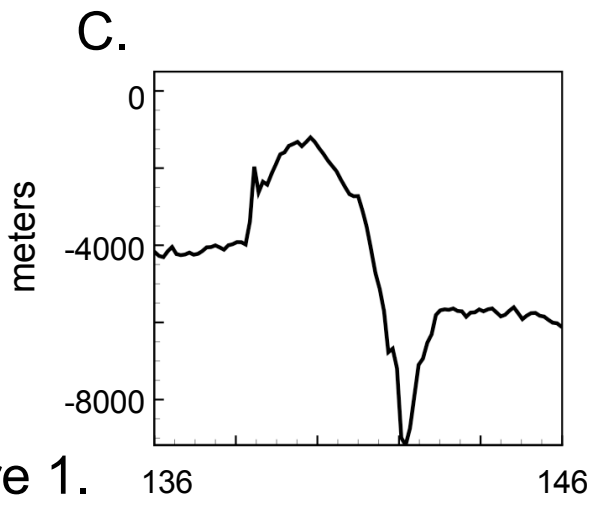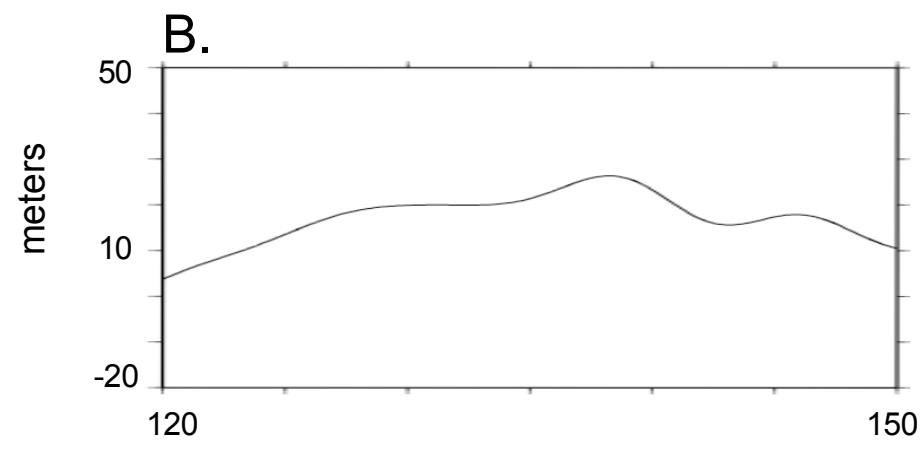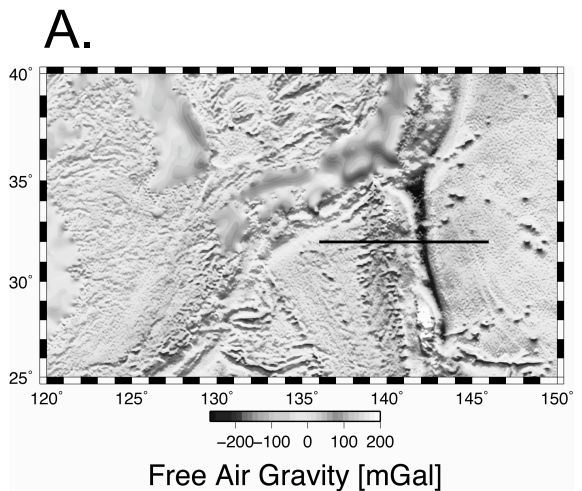
A.

Free Air Gravity [mGal]

−200 −100 0 100 200

B.

meters

50

10

−20

120   150

IV-34

C.

meters

0

−4000

−8000

136   146

D.

mGal

200

0

−300

136   146

Figure 1.

Figure 2.

T = 273 K constant temperature, no-slip

25 Ma

135 Ma

x

z

3000 km

10x40 km²

10x10 km²

10x40 km²

GyPSM-S calculation
subdomain
200 km x 400 km

40x40 km²

40x10 km²

40x40 km²

A.

T = 1773 K constant temperature, no-slip
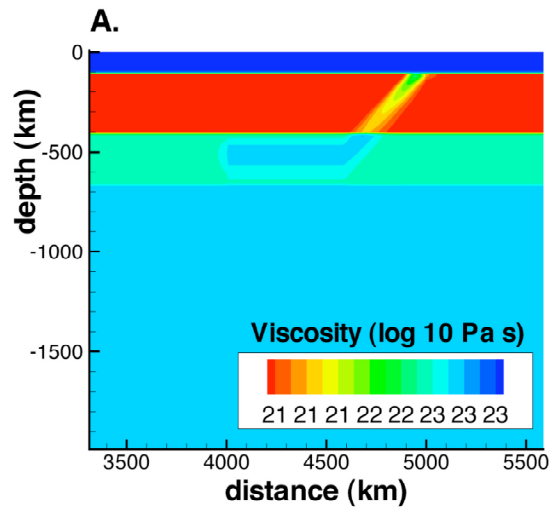
9000 km

Figure 3.

IV-36

Figure 4.

Figure 5.

IV-39
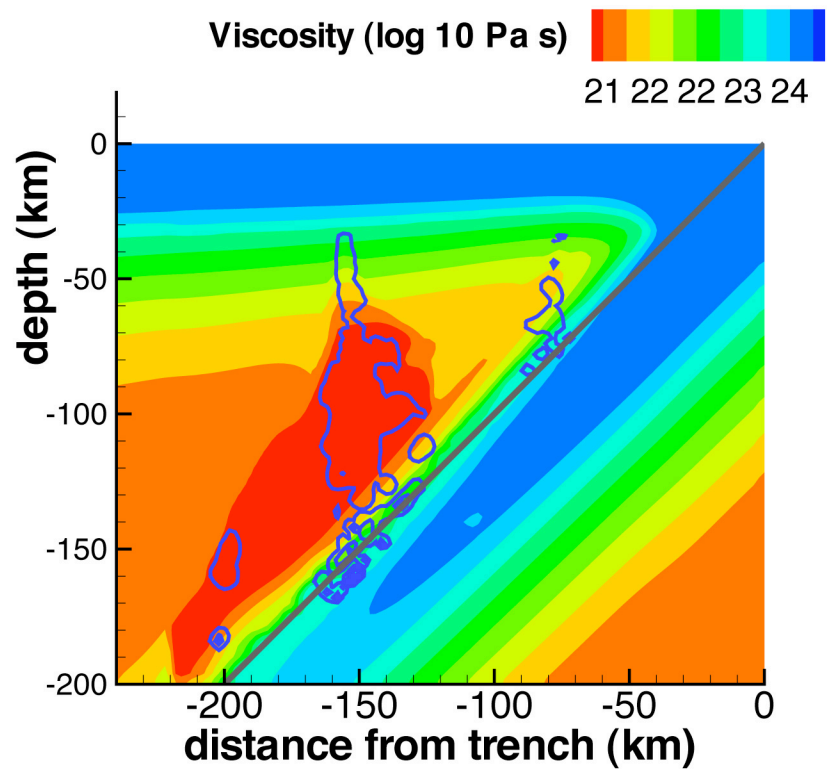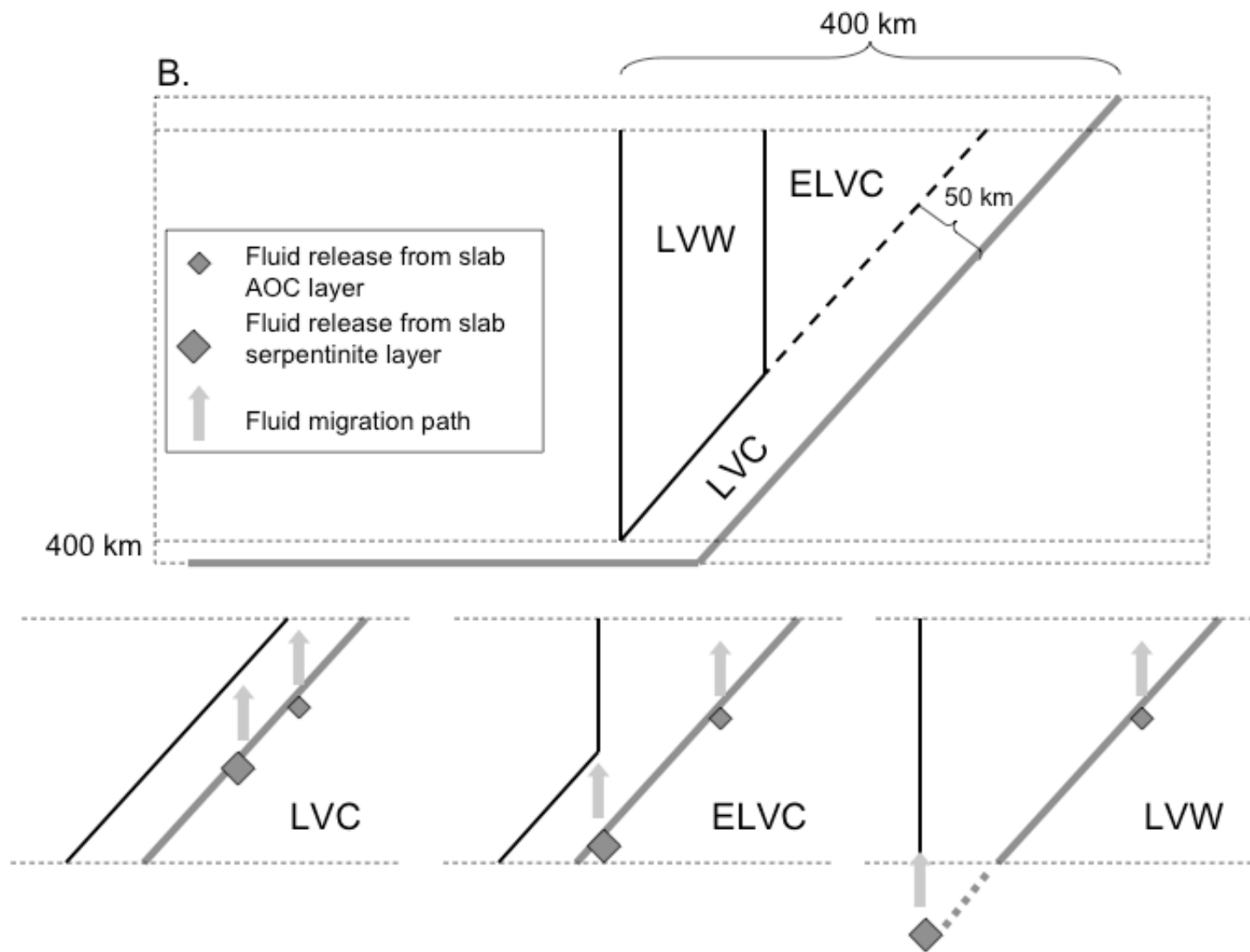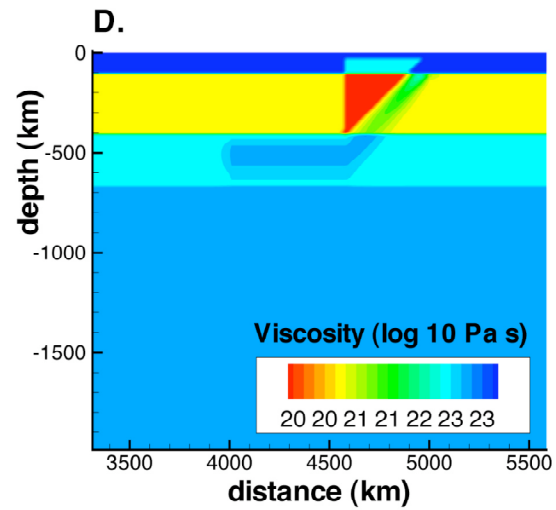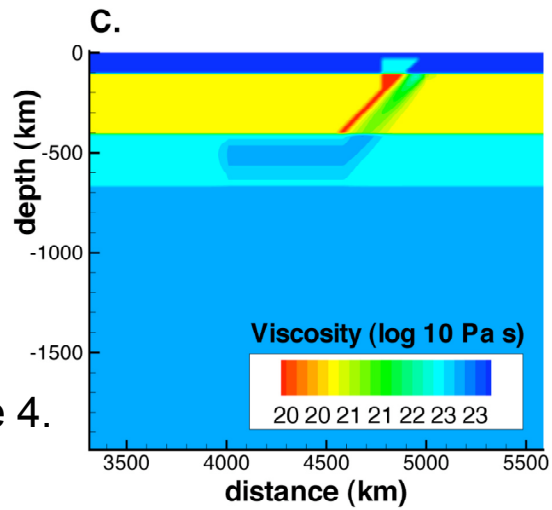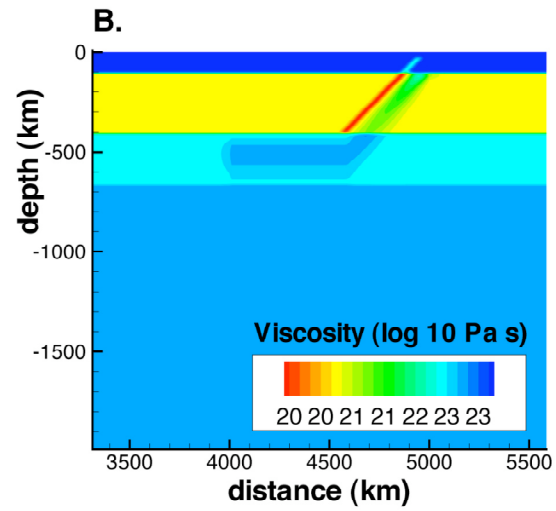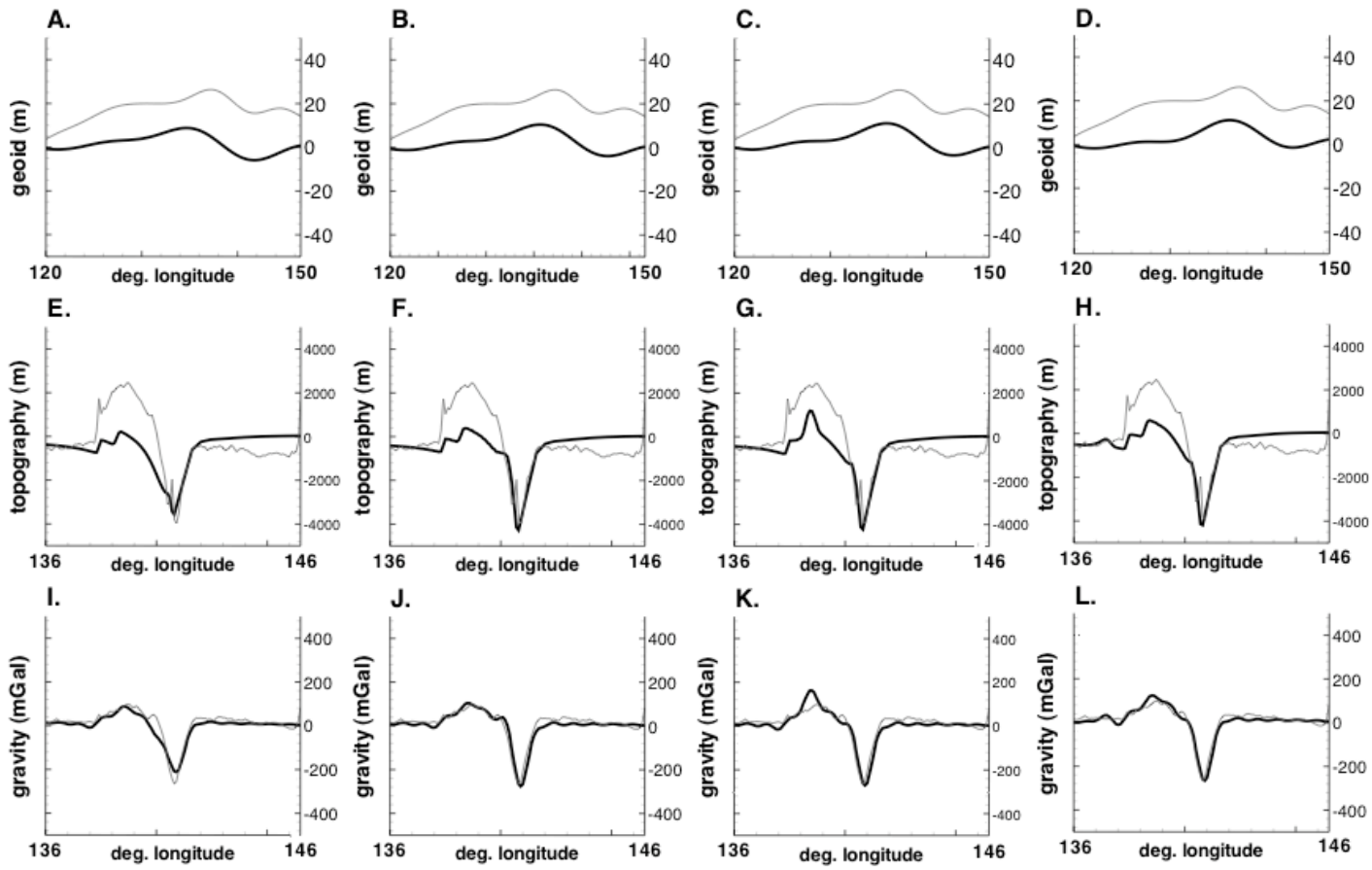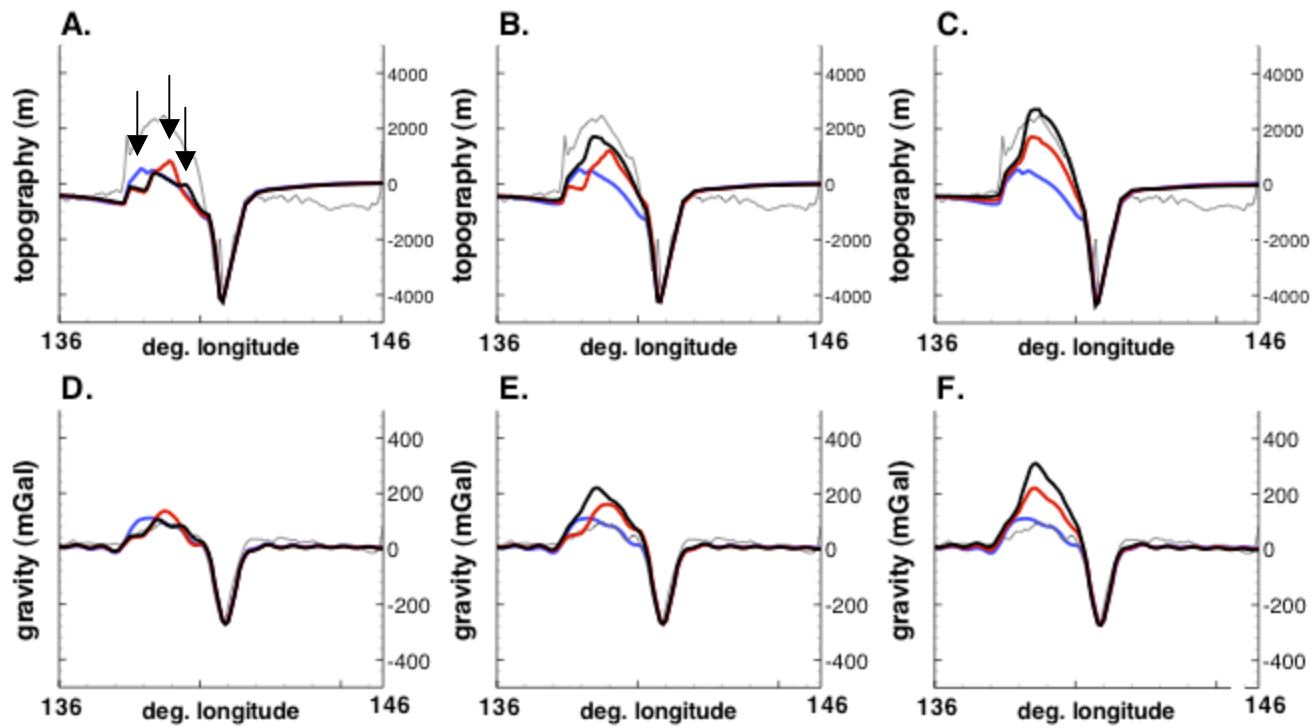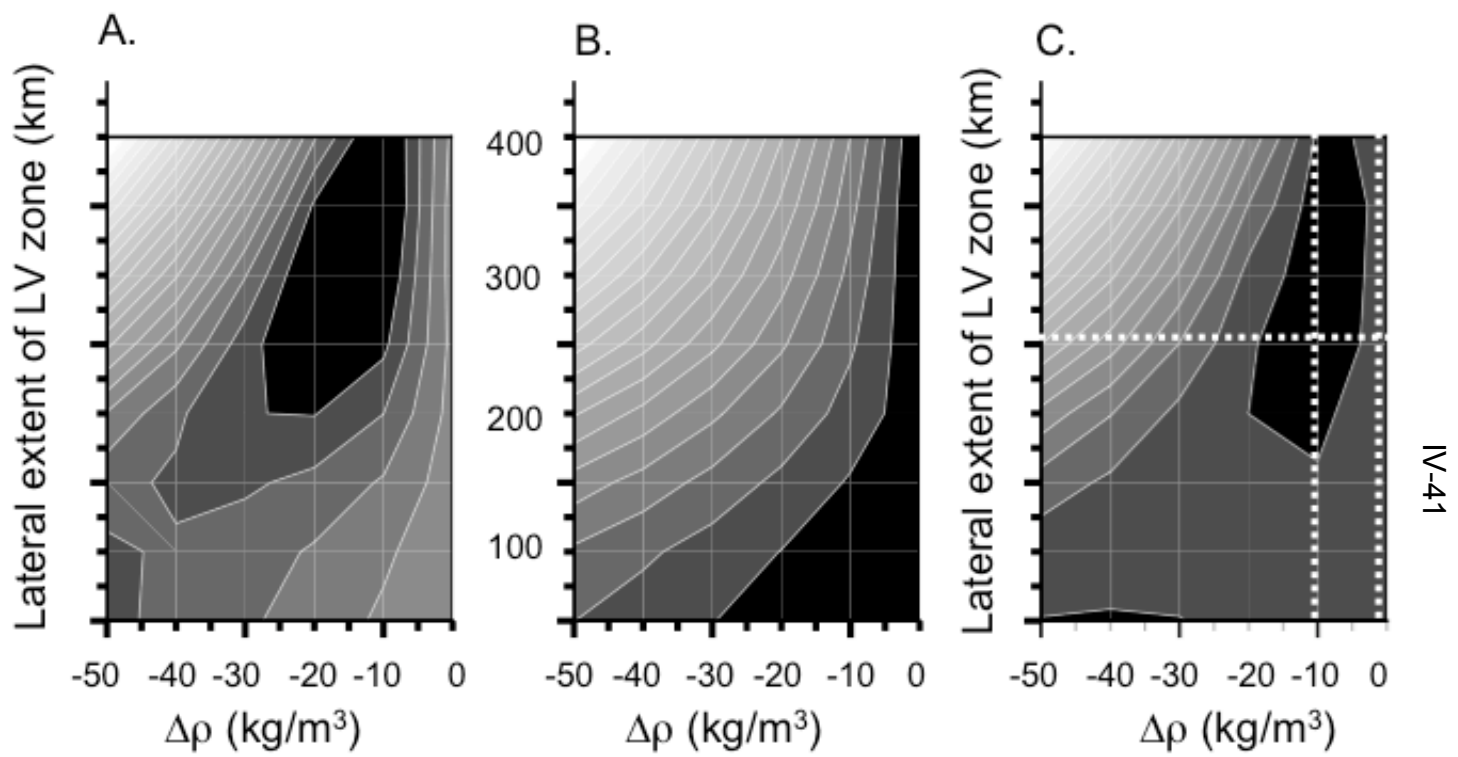
Figure 6.

Figure 7.

Table 1: Model parameters held constant

parameter	value	units
ΔT	1500	K
Ra	1.40E+08	*
η_0	3.0E+20	Pa s
Q	500	kJ/mol
$A_{Philippine}$	24 [53]	Myr
$A_{Pacific}$	141 [53]	Myr
κ	1.0E-06	m^2/s
α	2.5E-05	K^{-1}
g	10.0	m/s^2
G	6.67E-11	$N\ m^2/kg^2$
d	3000	km
R	8.31	J/K mol

dimensionless quantity
numbers in square brackets indicate references

Table 2: Summary of GyPSM-S subduction zone model parameters for initial calculation

subduction region	Northern Izu-Bonin
abbreviation	NIB
latitude range	~32 ºN
longitude range	~136-146 ºE
rate of convergence (mm/yr)	50.0 [30]
slab dip angle	45º
slab thermal age (Ma)	135 [30]
rigid lithospheric thickness (km)	32
thermal lithospheric thickness (km)	66

numbers in square brackets indicate references

Table 3: Summary of low-viscosity (LV) region model cases

model	depth extent of channel section (km)	depth extent of wedge section (km)	width of channel (km) from top of slab	width of wedge (km) at top	average water content in olivine (ppm)	$\Delta\rho$ (LVZ-wedge) (kg/m^3)
no LV	N/A	N/A	N/A	N/A	N/A	N/A
LVC1	400	0	50	0	1000	0
LVC2	400	0	50	0	1000	-10
LVC3	400	0	50	0	1000	-20
LVC4	400	0	50	0	1000	-50
ELVC1	400	100	50	100	1000	0
ELVC2	400	150	50	150	1000	0
ELVC3	400	180	50	180	1000	0
ELVC4	400	200	50	200	1000	0
ELVC5	400	200	50	200	2000	0
ELVC6	400	200	50	200	1000	-10
ELVC7	400	200	50	200	1000	-20
ELVC8	400	200	50	200	1000	-50
ELVC9	400	100	50	100	1000	-10
ELVC10	400	100	50	100	1000	-20
ELVC11	400	100	50	100	1000	-50
ELVC12	400	150	50	150	1000	-10
ELVC13	400	150	50	150	1000	-20
ELVC14	400	150	50	150	1000	-50
ELVC15	400	180	50	180	1000	-10
ELVC16	400	180	50	180	1000	-20
ELVC17	400	180	50	180	1000	-50
LVW1	400	300	50	300	1000	0
LVW2	N/A	400	N/A	400	1000	0
LVW3	400	300	50	300	1000	-10
LVW4	400	300	50	300	1000	-20
LVW5	400	300	50	300	1000	-50
LVW6	N/A	400	N/A	400	1000	-10
LVW7	N/A	400	N/A	400	1000	-20
LVW8	N/A	400	N/A	400	1000	-50
ELVC18	400	100	50	100	1000	-30
ELVC19	400	100	50	100	1000	-40
ELVC20	400	150	50	150	1000	-30
ELVC21	400	150	50	150	1000	-40
ELVC22	400	200	50	200	1000	-30
ELVC23	400	200	50	200	1000	-40
LVC5	400	0	50	0	1000	-30
LVC6	400	0	50	0	1000	-40
LVW9	400	300	50	300	1000	-30
LVW10	400	300	50	300	1000	-40
LVW11	N/A	400	N/A	400	1000	-30
LVW12	N/A	400	N/A	400	1000	-40
ELVC24	400	250	50	250	1000	0
ELVC25	400	250	50	250	1000	-10
ELVC26	400	250	50	250	1000	-20
ELVC27	400	250	50	250	1000	-30
ELVC28	400	250	50	250	1000	-40
ELVC29	400	250	50	250	1000	-50
LVW13	400	350	50	350	1000	0
LVW14	400	350	50	350	1000	-10
LVW15	400	350	50	350	1000	-20
LVW16	400	350	50	350	1000	-30
LVW17	400	350	50	350	1000	-40
LVW18	400	350	50	350	1000	-50

Table 4: Summary of benchmark cases

case	resolution (x,y)	Ra
bm1	32×32	10^5
bm2	64×64	10^5
bm3	64×64	10^4
bm3	64×64	10^6